

Chapter 9

Wind Tunnel Experiment and Large Eddy Simulation of Pollutant/Thermal Dispersion in Non-isothermal Turbulent Boundary Layer

Ryuichiro Yoshie

Abstract This chapter firstly describes the necessity of validation study of CFD in relation to pollutant/thermal dispersion in urban areas by comparing CFD results with reliable wind tunnel experimental data. The second section explains a technique for simultaneously measuring fluctuating velocity, temperature, and concentration in non-isothermal turbulent layers. The third section introduces examples of pollutant/thermal dispersion experiments in non-isothermal turbulent boundary layers with different atmospheric stability conditions. This measurement technique was used for the wind tunnel experiments. The fourth section reviews various methods for generating inflow turbulence for large eddy simulation and shows some calculated results by large eddy simulation of pollutant/thermal dispersion that target the wind tunnel experiments mentioned above with the experimental data.

Keywords Non-isothermal flow • Atmospheric stability • Pollutant dispersion • Wind tunnel experiment • Large eddy simulation

9.1 Introduction

With recent progress in high-speed processing of personal computers and propagation of commercial CFD software, it is becoming possible to predict pedestrian wind environments around actual high-rise buildings by CFD. In order to assure the quality of the CFD simulations, an AIJ (Architectural Institute of Japan) CFD working group conducted many comparative and parametric studies on various building configurations (Yoshie et al. 2007a). Based on these validation studies, the AIJ published “Guidelines for practical applications of CFD to pedestrian wind environment around buildings” in 2007 and 2008 (AIJ 2007 (Japanese version),

R. Yoshie (✉)
Tokyo Polytechnic University, Kanagawa, Japan
e-mail: yoshie@arch.t-kougei.ac.jp

Tominaga et al. 2008a (English version)). Since publication of the AIJ guidelines, application of CFD to environmental impact assessment of pedestrian wind for actual urban development is increasing in Japan.

The AIJ guidelines mainly targeted strong wind problems around high-rise buildings. Furthermore, rapid urbanization especially in Asian countries has been bringing about serious air pollution and urban heat island phenomena, which become more serious in weak wind conditions. The importance of urban ventilation in weak wind regions such as behind buildings and within street canyons is now broadly recognized as a countermeasure to the urban heat island phenomenon and air pollution problems. In such weak wind regions, buoyancy effect due to spatial temperature difference caused by solar and nocturnal radiations cannot be neglected. CFD is expected to become a useful tool to predict and assess these issues as well as strong wind problems. In order to apply CFD techniques to estimate ventilation and pollutant/thermal dispersion in urban areas, it is indispensable to assess calculation conditions and performance of turbulence models by comparing calculated results with experimental data. However, such validations of CFD for pollutant/thermal dispersion in non-isothermal turbulent boundary layers are quite rare in the wind engineering field. One reason is that few research institutes have wind tunnels that can control air temperature and surface temperature of ground (wind tunnel floor) and building models, and few reliable experimental data are available to validate CFD results. Wind velocity measurement by hot-wire anemometers in non-isothermal flows is difficult because output voltages from the hot wires are affected not only by wind velocity but also by temperature. Ohya measured wind velocity and temperature fluctuation simultaneously in a thermally stratified wind tunnel using an X-type hot wire and an I-type cold wire (Ohya 2001; Ohya and Uchida 2004). But it is difficult to apply their method to weak wind regions such as behind buildings and within street canyons where both positive and negative (reverse) flows exist. An X-type hot wire can measure wind velocity components only if no reverse flow occurs at any instantaneous moment. Furthermore, velocity, temperature, and concentration should be measured simultaneously to obtain turbulent heat fluxes and turbulent pollutant concentration fluxes, which are important turbulent statistics to validate CFD results. Laser Doppler velocimeter (LDV), which is not influenced by air temperature, may be used for simultaneous measurement. However, seeding particles for LDV measurement stuck to a cold wire or a thermocouple cause error in temperature measurement, and they can cause damage to instruments for pollutant concentration measurement. Thus, it is very difficult to measure wind velocity, temperature, and pollutant concentration simultaneously in non-isothermal turbulent boundary layers. This chapter describes a technique for simultaneously measuring fluctuating velocity, temperature, and concentration and introduces some results of validation studies on large eddy simulation of pollutant/thermal dispersion in non-isothermal boundary layers.

9.2 Technique for Simultaneously Measuring Fluctuating Velocity, Temperature, and Concentration

The authors (Yoshie et al. 2007b) have developed a system for simultaneously measuring fluctuating velocity, temperature, and concentration by refining and expanding Ohya's method (Ohya 2001; Ohya and Uchida 2004). This system is composed of a split film probe, a cold-wire thermometer, and a high-speed flame ionization detector and has the following characteristics:

1. Turbulent heat fluxes and turbulent concentration fluxes can be obtained from simultaneously measured instantaneous wind velocity, temperature, and concentration.
2. It is possible to distinguish between positive flow and negative (reverse) flow in weak wind regions by using a split film probe.
3. It achieves appropriate temperature compensation for the output voltage of the split film in a flow with a large temperature fluctuation.

9.2.1 Calibrator of Split Film Probe and Cold Wire

In order to precisely calibrate the split film probe and the cold wire under non-isothermal low wind speed condition, reference wind velocity and temperature and output voltages from the split film and the cold wire should be precisely measured under low turbulent conditions. Calibrators for the split film probe and the cold wire (Fig. 9.1) were developed for this purpose. A laminar flow meter precisely measures the flow volume rate inside the calibrator (diameter, $D = 100$ mm), and mean wind velocity in the calibration part, U_{mean} , is obtained by dividing the flow volume rate by the area of the cross section at the calibration part. Based on this U_{mean} , and by considering the wind velocity profile shown in Fig. 9.2 (discussed later), wind velocity around the center of the calibrator, U_c , is obtained. This U_c is the reference wind velocity used for calibration of the split film probe. A duct heater is used for temperature control, and the air temperature θ_a inside the calibrator is measured by a thermocouple with a wire diameter of $75 \mu\text{m}$.

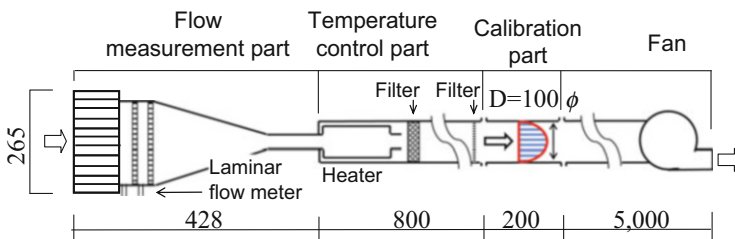


Fig. 9.1 Calibrator for split film probe and cold wire

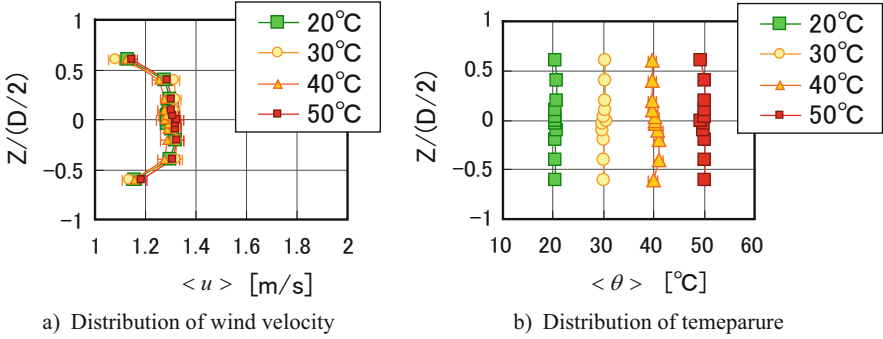


Fig. 9.2 Distribution of wind velocity and temperature inside calibrator

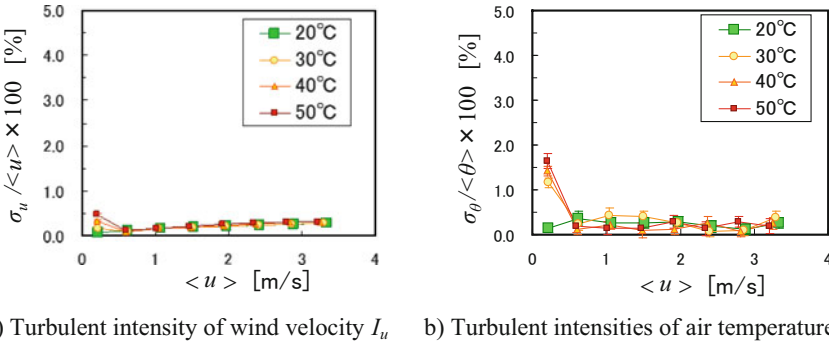


Fig. 9.3 Turbulence intensities of wind velocity and temperature

This θ_a is the reference air temperature used for calibration of the cold wire and the split film probe. Insulating material is used for the outer package of the calibrator to reduce heat loss and control the temperature distribution inside the calibrator.

Figure 9.2 shows distributions of wind velocity and air temperature inside the calibrator. In the figures, $\langle \rangle$ means time averaging, i.e., $\langle u \rangle$ and $\langle \theta \rangle$ are the time-averaged wind velocity and temperature, respectively. The distributions of wind velocity and air temperature are homogeneous around the center of the calibrator ($Z/(D/2) = 0$). Therefore, if the split film probe and the cold wire are placed around the center of the calibrator, error due to the sensor position is very small. Figure 9.3 shows the turbulence intensities of wind velocity, I_u , and turbulent intensities of air temperature, I_θ , at $Z/(D/2) = 0$. In the figure, σ_u and σ_θ mean standard deviations of wind velocity and temperature fluctuation, respectively. As shown, both turbulent intensities are very small: $I_u < 1\%$ and $I_\theta < 2\%$. Figure 9.4 shows the relative uncertainty (ISO 1993) of wind velocity using this calibrator, which is less than 1.5%. However, when a wind tunnel is used instead of the calibrator, it is about 5.0%. Thus, the calibrator greatly improves the reliability of the wind velocity calibration.

Fig. 9.4 Relative uncertainty of wind velocity measurement

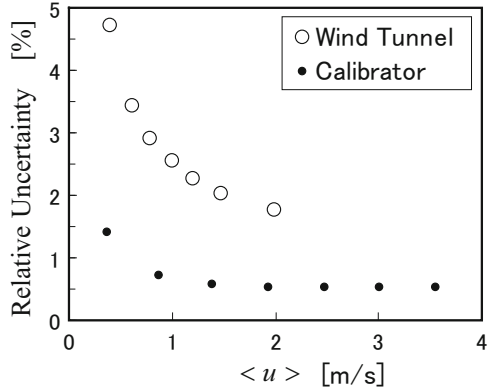
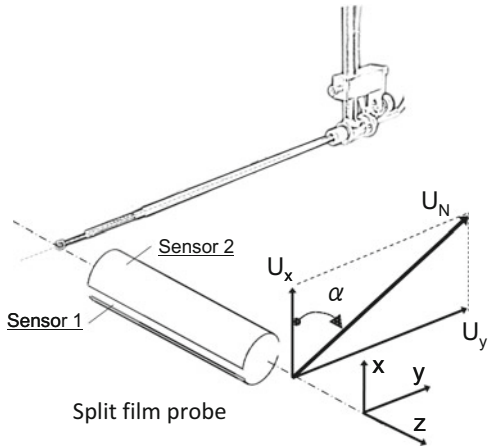


Fig. 9.5 Definition of coordinates of split film probe



9.2.2 Calibration Procedure for Cold Wire and Split Film Probe

In this measurement system, a split film probe of DANTEC (55R55 for u component, 55R57 for v component, 55R 56 for w component) and a CTA module (90C10) are adopted for wind velocity measurement; and a cold wire (55P31) and a temperature module (90C20) are used for temperature measurement. As shown in Fig. 9.5, the split film probe consists of two semicircular films which are split (insulated) from each other. The split film probe and the cold wire are placed at about 5 mm intervals in the calibrator so that the split film probe and the cold wire do not affect each other. The procedures for obtaining calibration data are as follows:

1. The angle of the wind approaching the split film probe is set as $\alpha = 0^\circ$ (Fig. 9.5) under a constant air temperature, and 8 values of reference wind velocity U_c are

used. For each wind velocity, the output voltages E_1 and E_2 from sensor 1 and sensor 2 of the split film probe are measured, and reference air temperature θ_a by the thermocouple and output voltage E_{cw} from the cold wire are measured.

2. The angle of the wind approaching the split film probe is set as $\alpha = 180^\circ$, and the above measurements are repeated.
3. The above procedures 1 and 2 are conducted for several reference air temperatures (e.g., 10–60 °C), to obtain E_1 , E_2 , and E_{cw} for each air temperature.

9.2.3 Calibration of Cold Wire

Figure 9.6 shows the relation between reference air temperature θ_a measured by the thermocouple and output voltage E_{cw} from the cold wire in the calibrator. As shown, E_{cw} changes linearly with θ_a and does not depend on wind velocity. Thus, the relation between E_{cw} and θ_a can be expressed as follows.

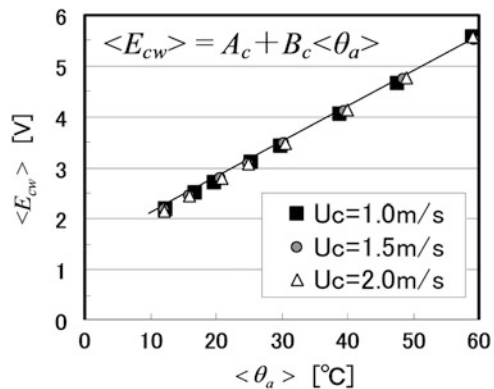
$$E_{CW} = A_c + B_c \theta_a \quad (9.1)$$

The calibration coefficients A_c and B_c (both constants) can be obtained by the least square method.

9.2.4 Measurement of Air Temperature in Wind Tunnel Experiment

In the wind tunnel experiments after the calibration procedure, instantaneous output voltage from the cold wire E_{cw} is measured and converted into instantaneous air temperature θ_a using the following equation, which is a deformation of Eq. (9.1).

Fig. 9.6 Relation between reference air temperature θ_a and output voltage E_{cw} from cold wire



$$\theta_a = \frac{E_{cw} - A_c}{B_c} \tag{9.2}$$

9.2.5 Calibration of Split Film and Measurement of Wind Velocity Components in Wind Tunnel Experiment

Figure 9.7 shows the relation between reference air temperatures θ_a measured by a thermocouple and the sum of squares of output voltages $\langle E_1 \rangle^2 + \langle E_2 \rangle^2$ from the split film in the calibrator. The surface temperature of the split film is kept at a fixed high temperature θ_s . As the air temperature θ_a increases, the difference between θ_a and θ_s becomes smaller, and the convective heat transfer from the split film to air decreases, and so the output voltages E_1 and E_2 from the split film become lower. The relation in Fig. 9.7 can be expressed by the following equation.

$$\langle \theta_a \rangle = \theta_s + C(\langle E_1 \rangle^2 + \langle E_2 \rangle^2) \tag{9.3}$$

Where C is a constant.

The intercept of this first-order approximation formula corresponds to the surface temperature of the split film θ_s , and it is obtained from the least square method.

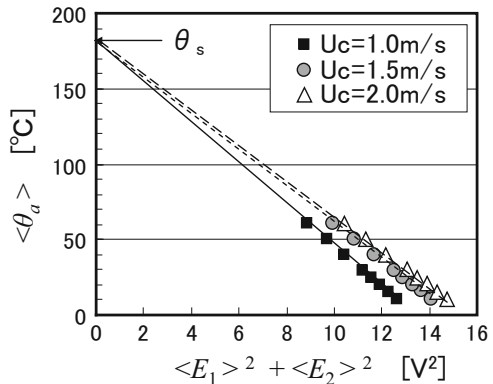
The relation between output voltages E_1 and E_2 from the split film probe and the reference wind velocity for calibration U_c can be expressed by the following equations based on King's law.

$$\frac{\langle E_1 \rangle^2 + \langle E_2 \rangle^2}{\theta_s - \langle \theta_a \rangle} = A_{(+)} + B_{(+)} \langle U_c \rangle^m \tag{9.4}$$

$$\frac{\langle E_1 \rangle^2 - \langle E_2 \rangle^2}{\theta_s - \langle \theta_a \rangle} = A_{(-)} + B_{(-)} \langle U_c \rangle^m \tag{9.5}$$

In Figs. 9.8a and b, the vertical axes represent the left-hand sides of Eqs. 9.4 and 9.5, respectively, and the horizontal axes depict $\langle U_c \rangle^m$. The value of m is specified

Fig. 9.7 Relation between reference air temperature and sum of squares of output voltages from split film probe



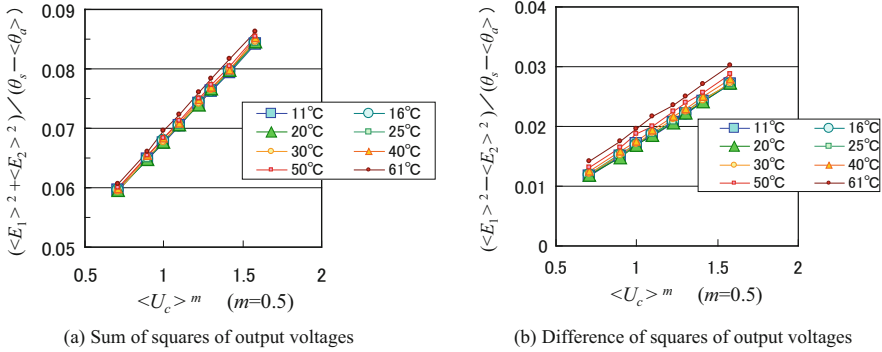


Fig. 9.8 Relation between output voltages of split film and reference wind velocity

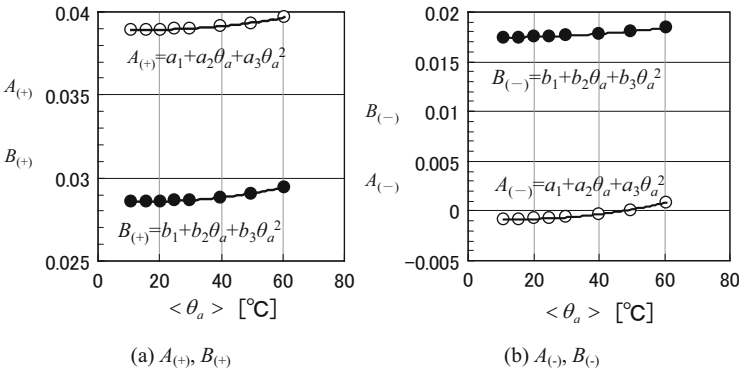


Fig. 9.9 Relation between calibration coefficients $A_{(+)}$, $B_{(+)}$, $A_{(-)}$, and $B_{(-)}$ and reference air temperature

so that the data can be best approximated by a linear function. In this calibration, $m = 0.5$. As shown in Fig. 9.8, since the calibration lines depend on air temperature θ_a , the calibration coefficients $A_{(+)}$, $B_{(+)}$, $A_{(-)}$, and $B_{(-)}$ become functions of θ_a , as shown in Fig. 9.9. Here, these coefficients are approximated by quadratic functions.

9.2.6 Measurement of Wind Velocity Components in Wind Tunnel Experiment

Figure 9.10 shows the relation between output voltages of the split film and the wind angle α to the split film (see Fig. 9.5).

In the wind tunnel experiments after the calibration procedure, calibration coefficients $A_{(+)}$, $B_{(+)}$, $A_{(-)}$, and $B_{(-)}$ for wind velocity are calculated from the instantaneous air temperature θ_a obtained from Eq. 9.2, and these calibration

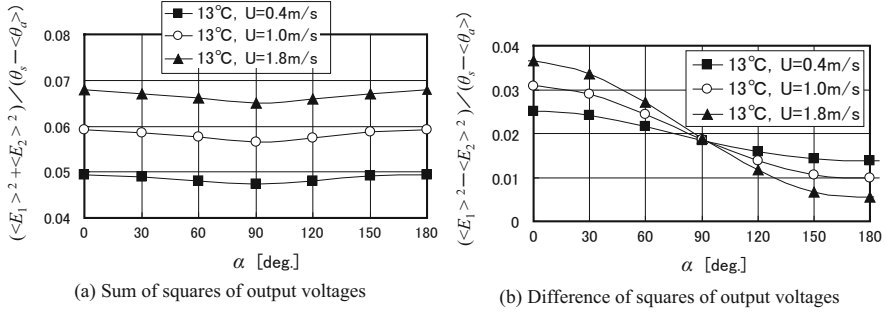


Fig. 9.10 Relation between output voltages of split film and wind angle

coefficients are used in the following procedures. The scalar wind velocity u_N can be obtained from

$$\frac{E_1^2 + E_2^2}{\theta_s - \theta_a} = A_{(+)} + B_{(+)}u_N^m \tag{9.6}$$

As shown in Fig. 9.10b, the difference between the squared split film’s output voltages C_α (Eq. (9.8)) can be approximated by a cosine curve, and so the instantaneous value of α is evaluated from Eq. 9.7:

$$\alpha = \begin{cases} \cos^{-1} \frac{C_\alpha - C_{90}}{|C_0 - C_{90}|} & \text{(for positive flow } (C_\alpha - C_{90} \geq 0)) \\ \cos^{-1} \frac{C_\alpha - C_{90}}{|C_{180} - C_{90}|} & \text{(for negative (reverse) flow } (C_\alpha - C_{90} < 0)) \end{cases} \tag{9.7}$$

where

$$C_\alpha = \frac{E_1^2 - E_2^2}{\theta_s - \theta_a} \tag{vertical axes in Fig. 9.8b and Fig. 9.10b} \tag{9.8}$$

$$C_0 = A_{(-),0} + B_{(-),0}u_N^m \tag{9.9}$$

where $A_{(-),0}$ and $B_{(-),0}$ are the calibration coefficients at $\alpha = 0^\circ$.

$$C_{180} = A_{(-),180} + B_{(-),180}u_N^m \tag{9.10}$$

where $A_{(-),180}$ and $B_{(-),180}$ are the calibration coefficients at $\alpha = 180^\circ$.

$$C_{90} = (C_0 + C_{180})/2 \tag{9.11}$$

The sum of squares of the split film’s output voltages shown in Fig. 9.10a has variation about 5 % among the cases of $\alpha = 0^\circ$, 180° , and 90° , and so scalar wind velocity u_N obtained from Eq. 9.6 is somewhat affected by wind angle α . Therefore, U_N and α that satisfy both Eqs. 9.6 and 9.7 are calculated using an iteration method, and then U_N and α are determined.

Using the determined instantaneous values of U_N and α , the instantaneous wind velocity components u_x and u_y are obtained by the following equations.

$$u_x = u_N \cos \alpha \tag{9.12}$$

$$u_y = u_N \sin \alpha \tag{9.13}$$

Figure 9.11 compares the scalar wind velocity $\langle u_N \rangle$ measured by this calibration method and that by an ultrasonic anemometer. In addition, Fig. 9.12 shows the measured value of $\langle C_\alpha - C_{90} \rangle / \langle C_{0,180} - C_{90} \rangle$ against the wind angle α , which is set by the angle controller. Both $\langle u_N \rangle$ and α are measured precisely, and their relative uncertainties are below 5 %.

Fig. 9.11 Measurement accuracy of scalar wind velocity

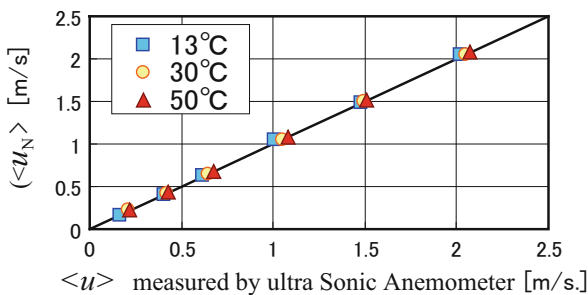


Fig. 9.12 Measurement accuracy of wind angle

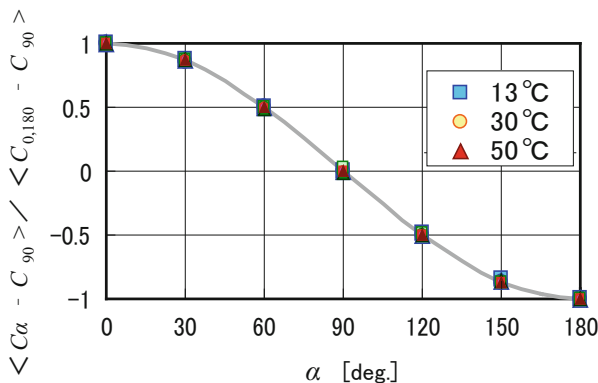
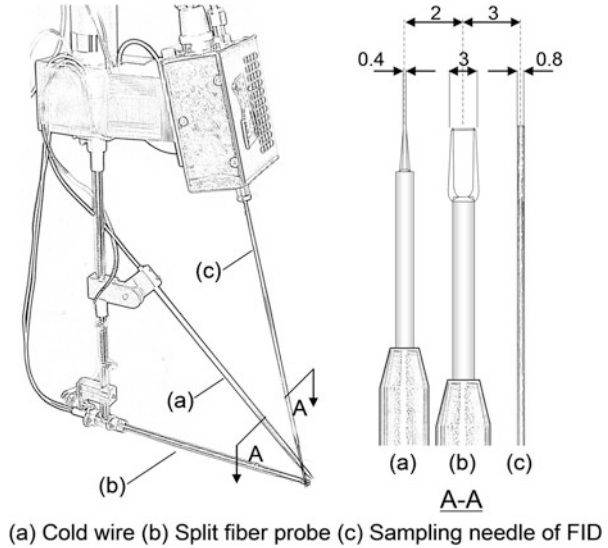


Fig. 9.13 Layout of sensors



9.2.7 Layout of Sensors in Wind Tunnel Experiment

In this system, it is necessary to place a split film, a cold wire, and a sampling tube of a high-speed flame ionization detector (FID) adjacent to one another. The influence of this layout on measured mean quantities and turbulent fluxes has been investigated (Yoshie et al. 2007b). Based on this investigation, the layout of sensors in the wind tunnel experiment was determined as shown in Fig. 9.13.

9.3 Examples of Wind Tunnel Experiments in Non-isothermal Turbulent Boundary Layer

9.3.1 Thermally Stratified Wind Tunnel

Figure 9.14 shows the thermally stratified wind tunnel in Tokyo Polytechnic University. This wind tunnel is a closed circuit type with a test section of 1.2 m wide, 1.0 m high, and 9.35 m long. The air is blown through a motor-driven fan of 5.5 kW DC. The maximum wind speed is 2.0 m/s at most because low wind speed is required to satisfy the similarity law of atmospheric stability condition.

The wind tunnel is equipped with a temperature profile cart (Fig. 9.15) and ambient air conditioners (Fig. 9.14). The air flow temperature can be controlled in the range of 10–60 °C by the temperature profile cart and ambient air conditioners. The temperature profile cart is installed between the contraction cone (contraction ratio=0.25) and the test section. It has four aluminum screens (opening

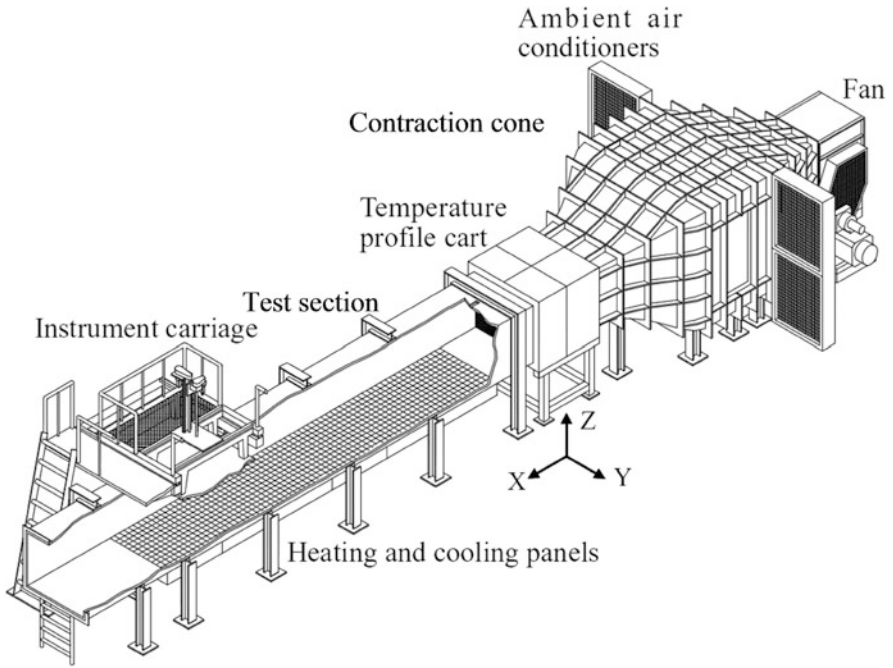


Fig. 9.14 Thermally stratified wind tunnel in Tokyo Polytechnic University

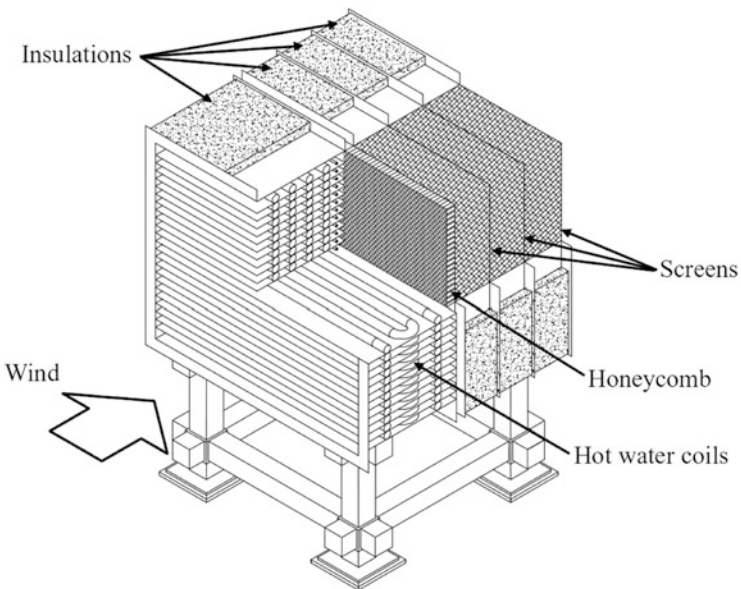


Fig. 9.15 Temperature profile cart

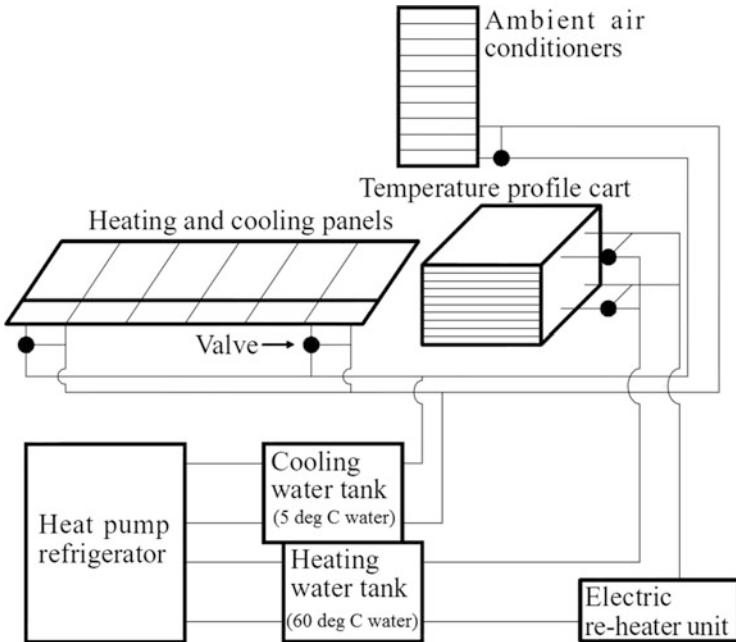


Fig. 9.16 Schematic diagram of temperature control systems

ratio = 61.5 %) at the diffuser section and a honeycomb after this section. The ambient air conditioners are responsible for maintaining the temperature outside the wind tunnel. This will maintain a uniform ambient temperature in the range of 8–20 °C. The floor of the test section consists of six heating and cooling panels with cooling coils and electric sheet heaters. The surface temperature of the floor can be controlled in the range between 10 °C and 80 °C.

Figure 9.16 is a schematic diagram of the temperature control systems of the wind tunnel. The temperature profile cart has hot water coils, and hot water is supplied from a heating water tank. This water is heated by an electric re-heater unit. The ambient air conditioners also have water coils for which cold water is supplied from the cooling water tank. Both the hot water and the cold water are generated by heat pumps. The cold water in the tank is also used for the cooling panels of the wind tunnel floor.

9.3.2 Wind Tunnel Experiment of Pollutant/Thermal Dispersion Behind a High-Rise Building

As shown in Figs. 9.15, 9.16, and 9.17, wind velocity, temperature, and gas concentration around a high-rise building within turbulent boundary layers with

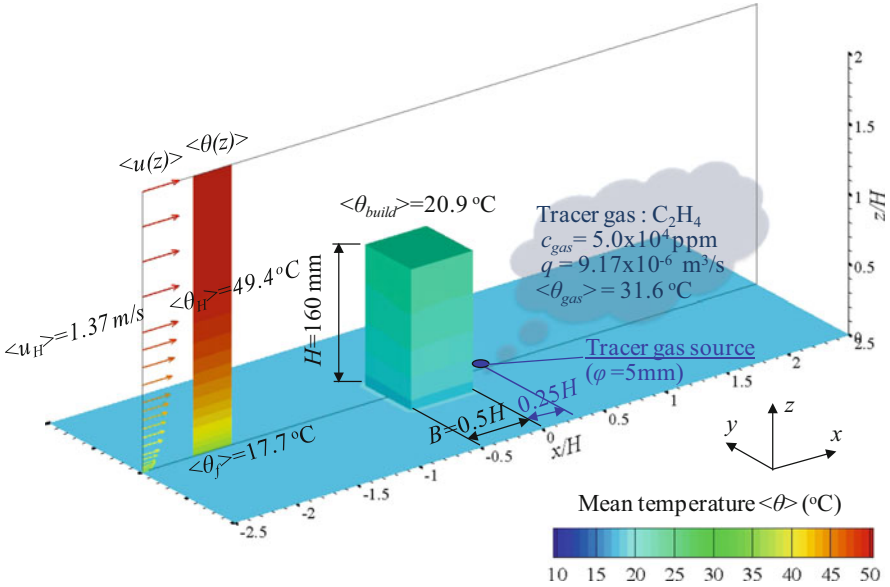


Fig. 9.17 Wind tunnel experiment on pollutant/thermal dispersion behind high-rise building within stable turbulent boundary layer

three different atmospheric stabilities (stable, neutral, and unstable) were measured using the technique described in Sect. 9.2. The purpose of this experiment was to produce data for CFD validation. The experiment was conducted in a thermally stratified wind tunnel in Tokyo Polytechnic University, shown in Fig. 9.14. The model building had a height (H) of 160 mm, a width (W) of 80 mm, and a depth (D) of 80 mm ($H, W, D = 2:1:1$) and was located in a turbulent boundary layer. The Reynolds number based on H (building height) and $\langle u_H \rangle$ (approaching wind velocity at building height) was about 15,000. A point gas source was set on the floor 40 mm leeward of the model building. Tracer gas (C_2H_4 , 5 % ethylene) was released from a hole (diameter, 5 mm) at a flow rate of $q = 9.17 \times 10^{-6} \text{ m}^3/\text{s}$. Table 9.1 summarizes the experimental conditions for the three atmospheric stability cases. The meanings of the symbols used in Figs. 9.17, 9.18, and 9.19 and Table 9.1 are described below.

- $\langle \zeta \rangle$: time averaged value of ζ
- ζ' : fluctuation from time-averaged value of ζ , $\zeta' = \zeta - \langle \zeta \rangle$
- $u, v, \text{ and } w$: three components of wind velocity [m/s]
- H : building height (0.16 m)
- u_H : approaching wind velocity at building height [m/s]
- θ : air temperature [$^{\circ}\text{C}$]
- θ_f : surface temperature of wind tunnel floor [$^{\circ}\text{C}$]
- θ_H : air temperature of approaching wind at building height [$^{\circ}\text{C}$]
- $\Delta\theta$: absolute value of temperature difference, $\Delta\theta = |\theta_H - \theta_f|$ [$^{\circ}\text{C}$]

Table 9.1 Experimental Conditions

Case	(a)	(b)	(c)
	Stable condition	Neutral condition	Unstable condition
R_b	0.08	0.00	-0.10
H [m]	0.16	0.16	0.16
$\langle u_H \rangle$ [m/s]	1.37	1.40	1.37
$\langle \theta_f \rangle$ [°C]	17.7	21.2	45.3
$\langle \theta_H \rangle$ [°C]	49.4	21.5	11.3
$\langle \Delta \theta \rangle$ [°C]	31.6	0.4	33.9
$\langle \theta_0 \rangle$ [°C]	41.9	21.5	16.6
$\langle \theta_{build} \rangle$ [°C]	20.9	21.1	41.7
$\langle \theta_{gas} \rangle$ [°C]	31.6	21.2	30.4

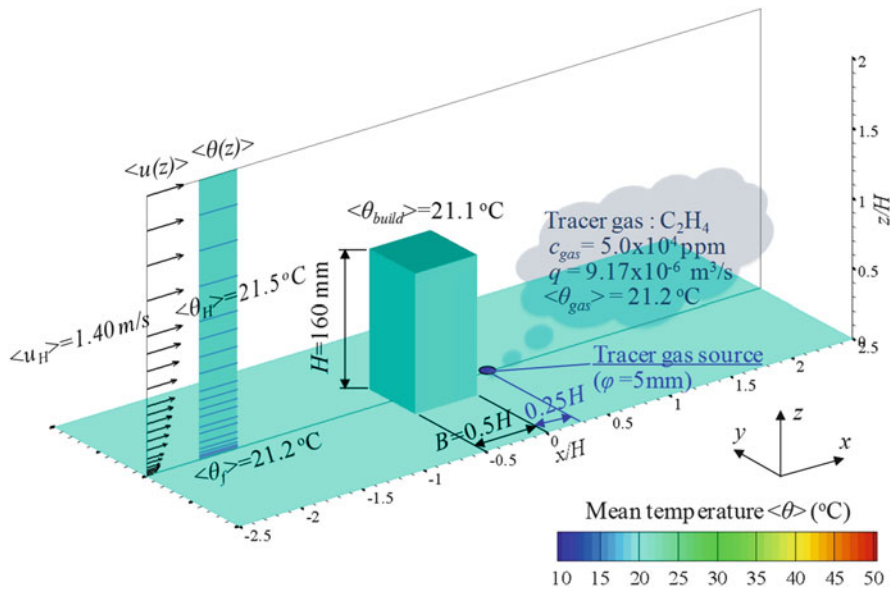


Fig. 9.18 Wind tunnel experiment on pollutant dispersion behind high-rise building within neutral turbulent boundary layer

- θ_0 : space-averaged air temperature in boundary layer [°C]
- θ_{gas} : temperature of released tracer gas [°C]
- θ_{build} : surface temperature of building model [°C]
- c : gas concentration (ppm)
- c_{gas} : released tracer gas concentration (5.0×10^4 ppm)
- q : released gas emission rate (9.17×10^{-6} m³/s)
- c_0 : reference gas concentration, $c_0 = c_{gas} q / \langle u_H \rangle H^2$ (ppm)
- Ri_b : Bulk Richardson number, $Ri_b = gH(\langle \theta_H \rangle - \langle \theta_f \rangle) / \{(\langle \theta_0 \rangle + 273) \langle u_H^2 \rangle\}$

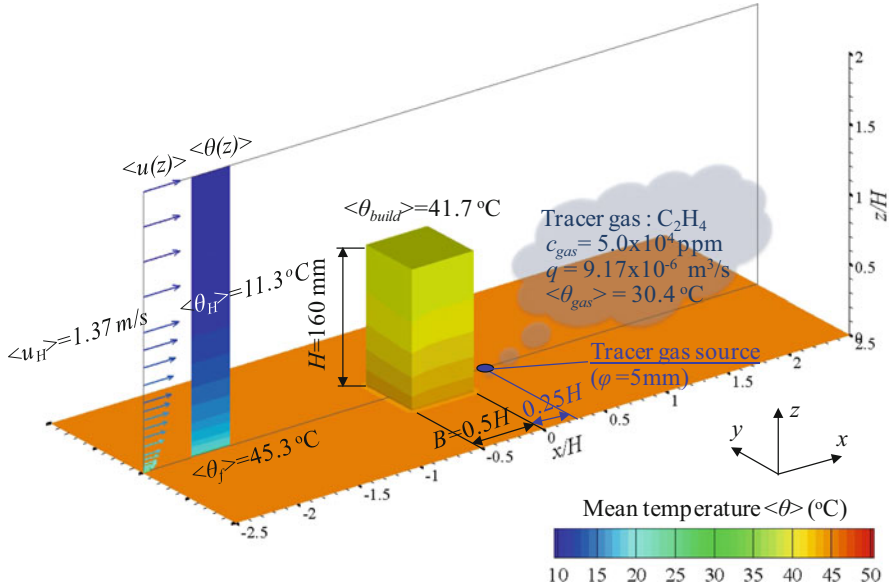


Fig. 9.19 Wind tunnel experiment on pollutant/thermal dispersion behind high-rise building within unstable turbulent boundary layer

The experimental database is open to the public on the website of Tokyo Polytechnic University (http://www.wind.arch.t-kougei.ac.jp/info_center/pollution/pollution.html).

The database includes the following quantities, which can be used for CFD validation.

- Mean wind velocity components: $\langle u \rangle / \langle u_H \rangle$, $\langle v \rangle / \langle u_H \rangle$, and $\langle w \rangle / \langle u_H \rangle$
- Mean scalar wind velocity: $\langle u_{sc} \rangle / \langle u_H \rangle$
- Normal stresses: $\langle u'^2 \rangle / \langle u_H^2 \rangle$, $\langle v'^2 \rangle / \langle u_H^2 \rangle$, and $\langle w'^2 \rangle / \langle u_H^2 \rangle$
- Shear stresses: $\langle u'v' \rangle / \langle u_H^2 \rangle$ and $\langle u'w' \rangle / \langle u_H^2 \rangle$
- Turbulent kinetic energy: $k / \langle u_H^2 \rangle$
- Mean temperature: $(\langle \theta \rangle - \langle \theta_f \rangle) / \langle \Delta \theta \rangle$
- Standard deviation of temperature: $\sigma_\theta / \langle \Delta \theta \rangle$
- Turbulent heat fluxes: $\langle u'\theta' \rangle / (\langle u_H \rangle \langle \Delta \theta \rangle)$, $\langle v'\theta' \rangle / (\langle u_H \rangle \langle \Delta \theta \rangle)$, and $\langle w'\theta' \rangle / (\langle u_H \rangle \langle \Delta \theta \rangle)$
- Mean concentration: $\langle c \rangle / c_0$
- Standard deviation of concentration: σ_c / c_0
- Turbulent concentration fluxes: $\langle u'c' \rangle / (\langle u_H \rangle c_0)$, $\langle v'c' \rangle / (\langle u_H \rangle c_0)$, and $\langle w'c' \rangle / (\langle u_H \rangle c_0)$

9.3.3 Wind Tunnel Experiment on Pollutant/Thermal Dispersion Within Building Block

The second example is a wind tunnel experiment on pollutant/thermal dispersion within a building block (Yoshie and Hu 2013). Figure 9.20 shows the experimental setup. This experiment was also conducted in a thermally stratified wind tunnel in Tokyo Polytechnic University shown in Fig. 9.14. The turbulent boundary layers were generated by 26 very thin roughness elements made of thin aluminum plates located upstream. They created a long, rough upwind fetch to generate a turbulent boundary layer.

A total of $9 \times 14 = 126$ cubic blocks was put in the turbulent boundary layer located downstream (Figs. 9.20 and 9.21) to represent building blocks. Each building block had the same configuration: L (60 mm) \times W (60 mm) \times D (60 mm). The city blocks were spaced 60 mm apart in both the x and y directions. Figure 9.21 shows an overview of the building block arrangement. Tracer gas ethylene (C_2H_4) was released from a line of the floor. Figure 9.22 shows measuring points. The locations of the measuring points were selected so that various flow patterns (reverse flow, upward flow, and downward flow in the street canyons and flow on the roads) were included.

The purpose of this wind tunnel experiment was to produce data for CFD validation and also to investigate the effect of atmospheric stability on pollutant concentration in a city. Thus, atmospheric stability was changed in five cases as shown in Table 9.2. The reference height H_R was 0.32 m, and the velocity at this height of inflow boundary was set as reference velocity (U_R). The atmospheric stability was characterized by Bulk Richardson number (Ri_b). Bulk Richardson number can be expressed as follows:

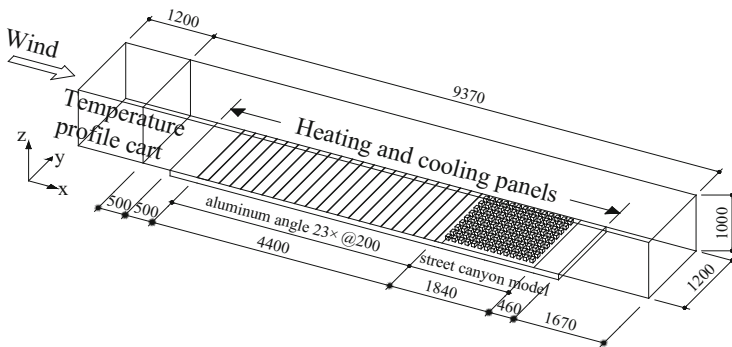


Fig. 9.20 Experimental setup (units, mm)

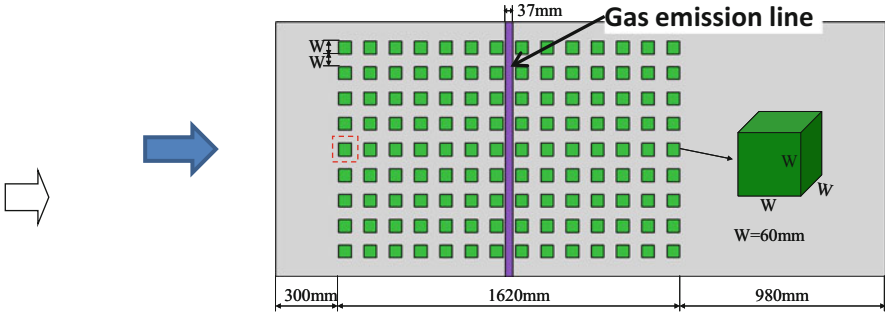


Fig. 9.21 Arrangement of building blocks

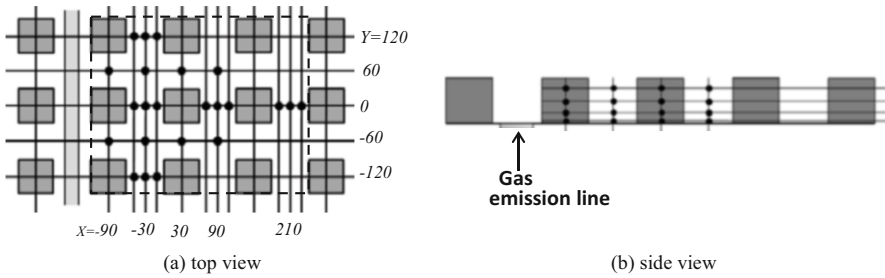


Fig. 9.22 Measuring points

Table 9.2 Atmospheric stability conditions

	Unstable	Weakly unstable	Neutral	Weakly stable	Stable
U_R [m/s]	1.4	1.8	1.8	1.5	1.2
θ_R [°C]	9	10	11	48	55
θ_f [°C]	49	41	11	16	14
$\Delta\theta$ [°C]	40	31	0	32	41
θ_0 [°C]	13	14	11	48	55
Ri_b	-0.23	-0.1	0	0.13	0.29

$$Ri_b = \frac{gH_R \times (\theta_R - \theta_f)}{(\theta_0 + 273) \times U_R^2}$$

where g is the acceleration due to gravity [m/s^2], H_R is the reference height [m], θ_R is the temperature at reference height [°C], θ_f is the surface temperature of the wind tunnel floor [°C], T_0 is the average inflow temperature [°C], and U_R is the velocity at reference height [m/s].

Ri_b for 5 inflow profiles are summarized in the last row of Table 9.2. Values of Ri_b ranged from -0.23 (unstable) to 0.29 (stable).

Figure 9.21 shows correlations for normalized nondimensional concentration C^* between neutral and non-neutral conditions. The normalized nondimensional concentration C^* is defined as follows:

$$C^* = \frac{CU_R H_R^2}{q}$$

where C is concentration [–] and q is emission rate of tracer gas [m^3/s].

As shown in Fig. 9.23, data are plotted almost on a single straight line. Thus, the ratio between C^* under non-neutral and neutral conditions were almost independent of the measurement locations. The slope of the line becomes larger with increase in Bulk Richardson’s number Ri_b . C^* under unstable conditions were smaller than C^* under neutral condition, and C^* under stable conditions were larger than C^* under neutral condition.

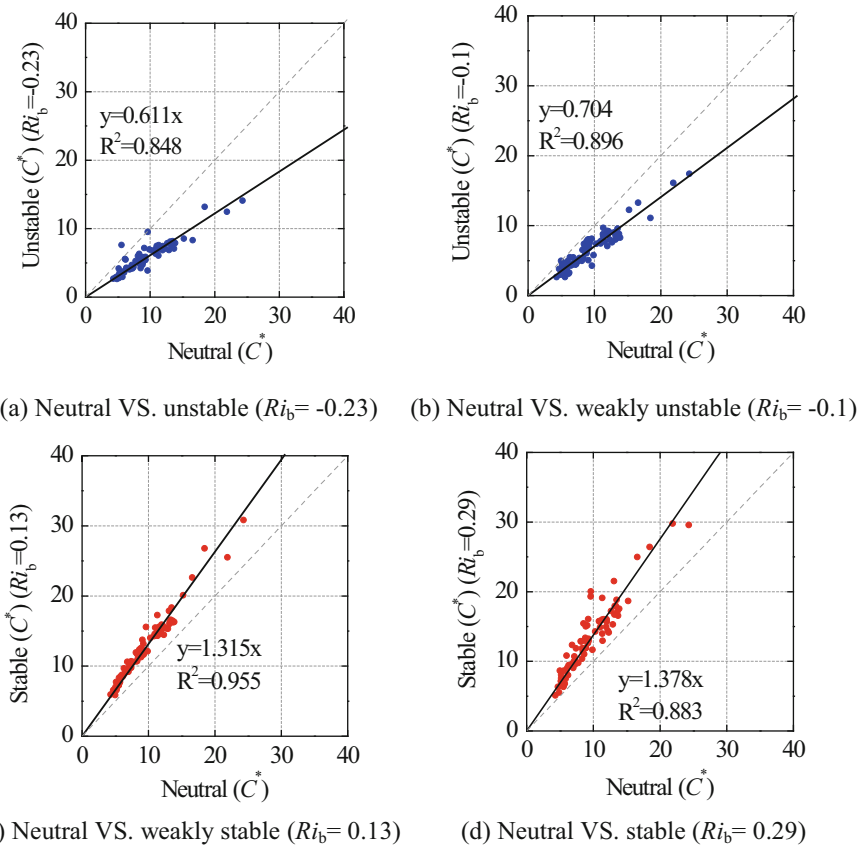


Fig. 9.23 Correlations of C^* between neutral condition and non-neutral conditions

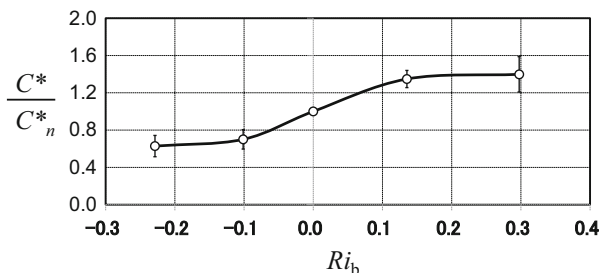


Fig. 9.24 Stability effect ratio (SER) = ratio between C^* under non-neutral condition and C_n^* under neutral condition

Figure 9.24 shows the ratio between C^* under non-neutral conditions and C_n^* under neutral condition obtained from the experiment. We call this stability effect ratio (SER) on pollutant concentration ($SER = C^*/C_n^*$). Averaged $SER \pm \sigma$ (standard deviation) of all the measuring points are plotted in the figure. As shown, with increase in Ri_b , the SER increases. Since the standard deviation is relatively small, the SER is almost independent of location. But further case studies are necessary with different configurations of the city model to confirm the generality of the SER. If the function of the SER is universal, we can predict pollutant concentration under non-neutral conditions from experimental results under neutral conditions by using the function.

9.4 Large Eddy Simulation of Pollutant/Thermal Dispersion in Non-isothermal Turbulent Boundary Layer

9.4.1 Generation of Inflow Turbulence for Large Eddy Simulation

Turbulent flows are complex states of fluid motion and are characterized by eddies with a wide range of length and time scales. When simulating turbulent atmospheric boundary layers using large eddy simulation (LES), a crucial issue is how to impose physically correct turbulence at the inflow boundary of LES. The incoming flow should have these spatial and temporal characteristics. The influence of inflow turbulence on large eddy simulation has been presented by Tominaga et al. (2008b). It has been confirmed that the inflow turbulence for LES is extremely important. Several techniques have been proposed for generating inflow turbulence for LES in a neutral boundary layer. Most of them can be classified into four basic categories: random noise (white noise), synthetic method, precursor simulation, and recycling method.

The simplest way is to superimpose random fluctuations on the mean velocity profile with amplitude determined by the turbulence intensity level. But due to the lack of the required characteristics of turbulent flow, random noise is not an appropriate inlet condition.

One commonly used way is the artificial generation method (synthetic method) in which velocity fluctuations are obtained from an inverse Fourier transform of a prescribed spectrum that satisfies the characteristics of power spectral density and spatial correlations of the turbulent boundary layer. A method of generating the inflow turbulence for computational wind engineering applications based on this approach was developed by Kondo et al. (1997), Maruyama et al. (1999), and Iizuka et al. (1999).

A digital-filter-based generation of turbulent inflow conditions was presented by Xie and Castro (2008), and the method was validated by simulating plane channel flows with smooth walls and flows over arrays of staggered cubes (a generic urban-type flow). Another synthetic method for generating realistic inflow conditions was presented by Druault et al. (2004) based on proper orthogonal decomposition (POD) and linear stochastic estimation (LSE). But its spatial resolution is not sufficient due to the limited number of hot-wire probes that simultaneously measure velocity. Perret et al. (2006) took the same approach based on the use of POD, but they coupled it with a database obtained by stereoscopic particle image velocimetry (SPIV).

Another method that has been used to generate inflow conditions involves running a separate precursor calculation of an equilibrium flow to generate a library of turbulent data that can be introduced into the main computation at the inlet (Tabor and Baha-Ahmadi 2010). This has the advantage that the inflow conditions for the main computation are taken from a genuine simulation of turbulence and thus should possess many of the required characteristics, including temporal and spatial fluctuation with correlation and a correct energy spectrum.

Instead of simulating the entire upstream region using precursor simulation, the most commonly used way is to employ a recycling method in which the velocity in a downstream plane is used (recycled) for the inflow boundary. In this method, the region used to generate turbulence is usually referred to as “driver region,” and the second region that we are interested in is usually referred to as “main region.” Lund et al. (1998) first proposed this rescaling recycling method to generate developing turbulent inflow data for LES. Kataoka and Mizuno (2002) simplified Lund’s method by assuming that the boundary layer thickness is constant within the driver section. Nozawa and Tamura (2002, 2005) extended Lund’s method to a rough-wall boundary layer flow using a roughness block arrangement. Now these methods are widely used to generate inflow turbulence for LES in neutral boundary layers.

The non-isothermal boundary layer (unstable or stable) is a very common atmospheric phenomenon, but there have been few LES studies on stratified atmospheric flows. When LES is applied to a non-isothermal field, not only inflow velocity fluctuation but also temperature fluctuation is necessary. Kong et al. (2000) proposed a method for generating inflow temperature fluctuation with reference to Lund’s method according to the similarity between temperature and stream-wise

velocity. To the author's knowledge, this is the first time inflow turbulence in the non-isothermal condition has been dealt with. In this method, the velocity fluctuation was generated using Lund's method, and the inflow temperature fluctuation was generated using the same rescaling and recycling law as that used for streamwise velocity. Hattori et al. (2007) conducted an unstable and stable boundary layer simulation, and the turbulent inflow data were generated by this method (Lund et al. 1998; Kong et al. 2000). In their calculation, the bulk Richardson number was -0.01 for the unstable condition and 0.01 for the stable condition, which corresponds to very weak thermal stratification. In the driver region, the neutral boundary layer was simulated, and the temperature was treated as a passive scalar.

Tamura et al. (2003) proposed a method for dealing with the thermally stratified effect. In the driver region, velocity fluctuation was generated using the quasi-periodic boundary condition for a rough wall, while temperature was treated as a passive scalar, and a mean temperature profile was given to the inflow condition of the driver region. Generated inflow data for temperature as well as velocity were introduced into the main computation domain, where the solution of physical quantities took into account buoyancy effects. But they also pointed out that fluctuation of the passive scalar was too large and not appropriate for the inflow condition of a stable turbulent boundary layer. Therefore, for stable conditions, the generated inflow velocity data at the recycling station were introduced into the main computational region, but a mean temperature profile without fluctuation was imposed at the inflow boundary of the main region (Tamura 2008). In the simulation of the urban heat island phenomena of the downtown region of Tokyo, as the flow coming from the sea was cold air, they used two driver regions to generate inflow turbulence for LES (Tamura et al. 2006). The driver region in domain 1 generated a neutral turbulent boundary layer by using the rescaling technique, and domain 2 thermally stabilized the turbulent boundary layer based on the sea breeze characteristics. Then the generated data were used for domain 3 to simulate the urban heat island phenomena of Tokyo. Abe et al. (2008) conducted LES calculation of gas dispersion in a convective boundary layer (CBL) and investigated the characteristics of turbulence structures and gas dispersion behavior. The inflow velocity and temperature fluctuations were generated using the method described by Tamura et al. (2003) for unstable boundary layers.

Brillant et al. (2008) also developed a thermal turbulent inflow condition based on parallel flows in order to simulate a turbulent thermal boundary layer. Then they tested this thermal turbulent inflow condition through a turbulent plane channel simulation. In this simulation, when velocity and temperature inflow fluctuations were given simultaneously, the fluctuating temperature profiles were well maintained as the flow proceeded downstream. If velocity inflow fluctuation and only a mean temperature profile (no fluctuation) were given as inflow condition, the temperature fluctuation gradually developed as the flow proceeded downstream. But the turbulent velocity field did not quickly generate thermal fluctuations.

Yoshie et al. (2011) used a precursor method to generate velocity and temperature fluctuations simultaneously in a non-isothermal boundary layer. In this method, the total simulations were composed of two domains: a pre-simulation

domain to generate inflow velocity and temperature fluctuations for LES and a main domain to simulate gas dispersion around a high-rise building in a non-isothermal boundary layer. In the pre-simulation, the whole wind tunnel and all the aluminum plates (roughness elements) were reproduced by large eddy simulation using a buoyant solver. As a continuation of the study, which only focused on an unstable case using a precursor method, Yoshie et al. (2011) and Jiang et al. (2012) investigated two inflow turbulence generation methods (precursor method and recycling method) in both unstable and stable boundary layers.

Okaze and Mochida (2014) proposed a new method of generating turbulent fluctuations of wind velocity and scalar parameters such as temperature and pollutant concentration based on the Cholesky decomposition of Reynolds stresses and turbulent scalar fluxes by expanding the methods of Xie and Castro (2008).

However, these kinds of researches on large eddy simulation of non-isothermal turbulent boundary layers are still quite rare, and methods of generating temperature fluctuation have not been sufficiently examined yet. Further investigations are anticipated.

9.4.2 Validation of Large Eddy Simulation of Pollutant/Thermal Dispersion in Non-isothermal Boundary Layer

This section introduces some of the validation studies on large eddy simulation of pollutant/thermal dispersion in an unstable boundary layer conducted by the authors.

9.4.2.1 Generation of Inflow Turbulence of Wind Velocity and Temperature for Large Eddy Simulation

Wind tunnel experiments described in Sects. 9.3.2 and 9.3.3 used the same experimental setup for producing a turbulent boundary layer, i.e., 26 very thin aluminum plates 9 mm high placed at $L = 200$ mm pitch on the wind tunnel floor as shown in Fig. 9.25.

Two turbulence generation techniques (precursor method and recycling method) were examined to reproduce the turbulent boundary layer shown in Fig. 9.25 (Jiang et al. 2012). Then the generated turbulence data were used for the inflow boundary condition for LES of gas/thermal dispersion behind a high-rise building (see Sect. 9.3.2) and within a street canyon (see Sect. 9.3.3) in an unstable turbulent boundary layer.

Firstly, a method for generating both velocity and temperature fluctuations simultaneously in non-isothermal boundary layers by precursor simulation is discussed here. In a previous study by Ohya and Uchida (2008), they simulated a

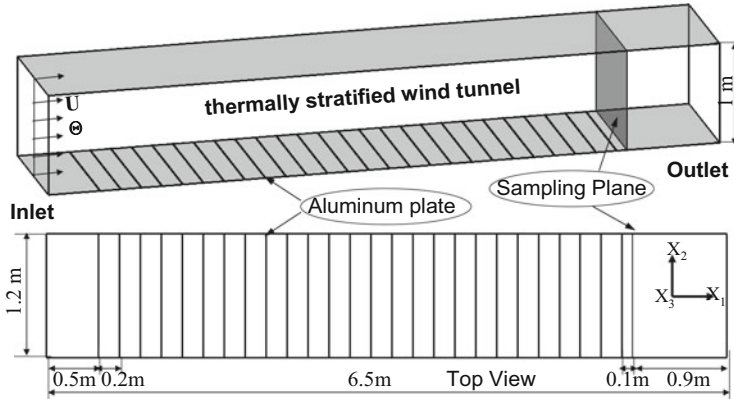


Fig. 9.25 Experimental setup for producing turbulent boundary layer (Jiang et al. 2012)

very long atmospheric boundary layer and investigated the influence of thermal stability on turbulence. We also simulated a long spatially developing turbulent boundary layer (including the transition from laminar flow to turbulent flow) but focused on the purpose of generating inflow turbulence for LES. In the precursor simulation, the whole wind tunnel and all the aluminum plates (Fig. 9.25) were reproduced by LES using a buoyant solver. The plates were treated as having zero thickness in the simulation. The wind velocity and temperature distribution at the inlet of the wind tunnel were spatially uniform, and turbulent intensity was very small (less than 1%), so a uniform velocity $U = 1.43$ m/s and a uniform temperature $\Theta = 9.4$ °C without turbulence were given to the inflow boundary of the pre-simulation. A zero gradient condition was used for the outlet boundary condition. A no-slip boundary condition was applied to the wall shear stress on the floor. The nondimensional distances from the surfaces to the first fluid cells were below 1.0 for most regions. As thermal boundary conditions, the surface temperature was 45.3 °C, and a heat conduction boundary condition (Fourier's law) was applied for the heat flux on the floor surface. The sampling plane to obtain fluctuating velocity and temperature data was set at 0.1 m (11 times the aluminum plate height) downstream of the last aluminum plate.

Another method for generating inflow turbulence in a non-isothermal boundary layer using a recycling procedure was also investigated here (Fig. 9.26). Tamura et al. (2003) proposed a method for dealing with the thermally stratified effect. In the driver region, velocity fluctuation was generated using Lund's method (Lund et al. 1998) for a rough wall, while temperature was treated as a passive scalar, and a mean temperature profile was given to the inflow condition of the driver region. The same concept was adopted here, but the velocity fluctuation was generated using Kataoka's method (Kataoka and Mizuno 2002) with the roughness ground arrangement described by Nozawa and Tamura (2002). The roughness elements were exactly the same as those used in the wind tunnel experiment, but a short domain was adopted here. A mean velocity profile that came from the experimental

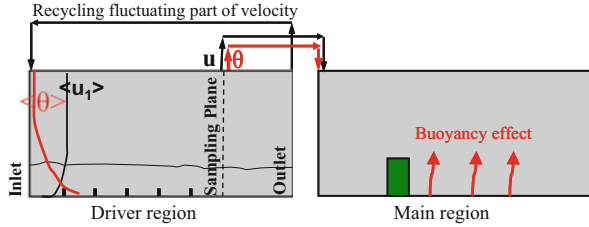


Fig. 9.26 Inflow turbulence generation by recycling method

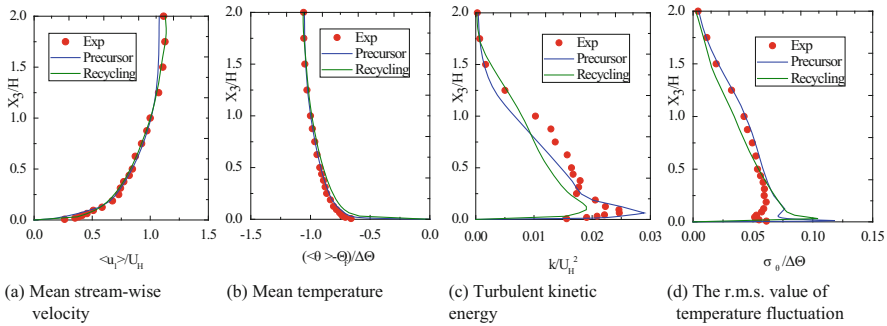


Fig. 9.27 Properties of generated turbulent flow by precursor and recycling methods

measurement was prescribed for the inflow condition, and only the fluctuating part was recycled between outlet station and inlet station. The following damping function (Kataoka 2008) was used to restrain development of the velocity fluctuation:

$$\varphi(\eta) = \frac{1}{2} \left\{ 1 - \tanh \left[\frac{8.0(\eta - 1.0)}{-0.4\eta + 0.82} \right] / \tanh(8.0) \right\} \tag{9.14}$$

where $\eta = z/\delta$. δ is the boundary layer thickness (0.25 m). Only a neutral boundary layer (NBL) was simulated in the driver region, the temperature was treated as a passive scalar, a mean temperature profile of the experiment was prescribed at the inflow boundary of the driver section, and we tried to use the fluctuating velocity field to generate a fluctuating temperature field.

Figure 9.27 shows the properties of generated flow by both the precursor method and the recycling method in the sampling position. The mean wind velocity, mean temperature, turbulent kinetic energy, and the r.m.s. value of temperature fluctuation agreed well with those of the experiment. Both methods can be used to generate turbulent inflow data for LES in an unstable boundary layer.

9.4.2.2 Examples of Large Eddy Simulation of Gas/Thermal Dispersion in Unstable Turbulent Boundary Layer

The generated inflow turbulence data were saved in a hard disk and used for an inflow boundary condition of LES for gas/thermal dispersion behind a single building (see Sect. 9.3.2) and within street canyons (see Sect. 9.3.3).

Firstly, LES results and experimental data of gas/thermal dispersion behind a single building within unstable turbulent boundary layer are compared (Yoshie et al. 2011).

Mean stream-wise velocities $\langle u_1 \rangle$ of the experiment and the calculations are shown in Fig. 9.28. The results from the RANS model (two-equation heat-transfer model (Nagano and Kim 1988)) show overestimation of the recirculation size behind the building, and the calculated downward flow in the region around $X_1/H = 0.7-1.5$ is weaker than the experimental one. The calculated reverse flow near the ground and the rising flow along the rear surface of the building are stronger than those of the experiment. On the other hand, the recirculation size by LES is narrower and the reverse flow near the ground and the rising flow along the rear surface of the building are weaker than those of the RANS model, which is closer to the experimental results.

Figures 9.29 and 9.30 show the distributions of mean gas concentration. In the RANS calculation result, the high concentration area near the ground does not spread downwind of the gas emission point (marked as a “black triangle”). Calculated gas concentration along the rear surface of the building was higher due to the rising flow from the ground. The calculation does not reproduce the periodic

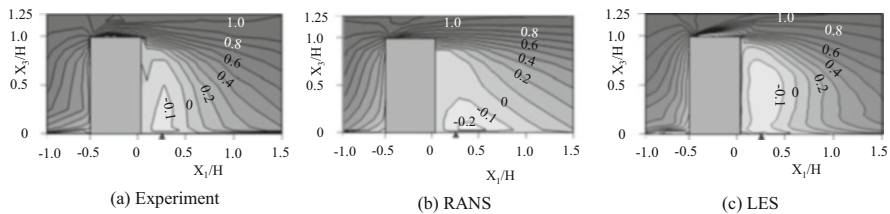


Fig. 9.28 Vertical distribution of mean velocity $\langle u_1 \rangle / U_H$ (Yoshie et al. 2011)

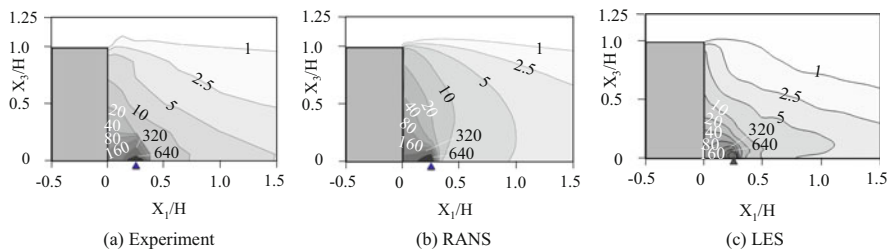


Fig. 9.29 Vertical distribution of mean concentration $\langle c \rangle / C_0$ (Yoshie et al. 2011)

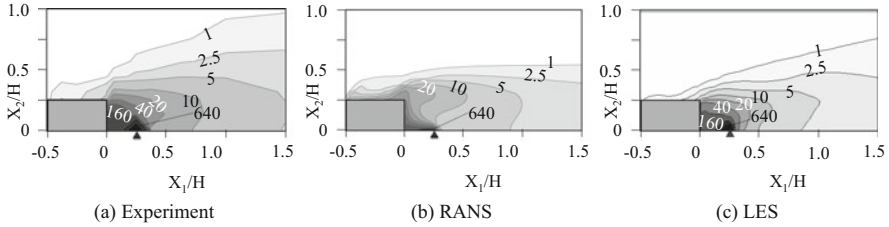


Fig. 9.30 Horizontal distribution of mean concentration $\langle c \rangle / C_0$ (Yoshie et al. 2011)

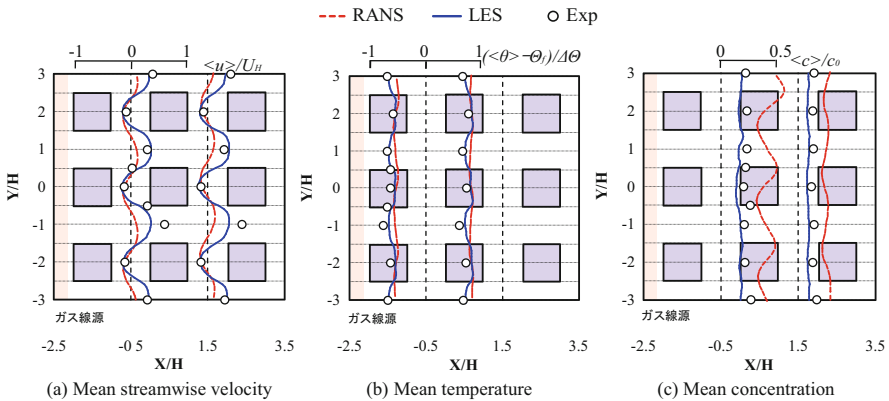


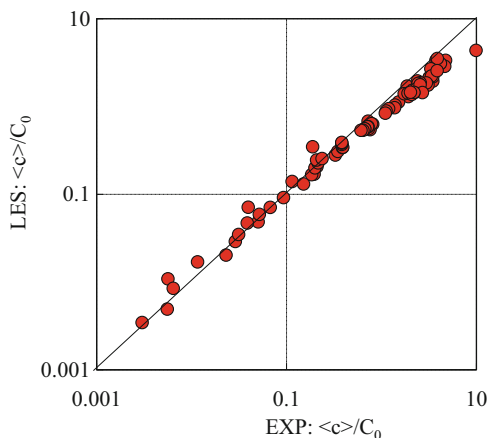
Fig. 9.31 Comparison between experimental result and CFD results ($z = H/6$)

fluctuations due to vortex shedding, and as a result, dispersion in the X_2 direction (lateral direction) is inhibited (Fig. 9.30). The distribution pattern of the LES is much closer to that of the experiment than of the RANS model, especially regarding the lateral width of gas dispersion.

Secondary, large eddy simulation of pollutant/thermal dispersion within a building block in an unstable turbulent boundary layer which targets the wind tunnel experiment described in Sect. 9.3.3. “Unstable” case in Table 9.2 was calculated by LES, and the results were compared with the experimental data.

Figure 9.31 shows the distributions of mean stream-wise velocity, mean temperature, and mean concentration near the floor ($z = H/6$ and H is building height). The LES results agreed well with the experimental data especially for the mean concentration. The RANS model (with standard $k-\epsilon$ model) overestimated the concentration by about 200 %. This is because the intermittent air exchange between street canyon and upper atmosphere cannot be reproduced in RANS, while it is well captured by LES. Figure 9.32 shows the correlations of mean concentration between experiment and LES results. The LES results are very close to the experimental data.

Fig. 9.32 Correlation between measured concentration and calculated concentration by LES



9.5 Conclusion

CFD is very promising for predicting and assessing air pollution and heat island phenomena in urban areas. Both phenomena have become serious problem especially in Asian countries with the rapid advance of urbanization. In order to appropriately apply CFD techniques to estimate ventilation and pollutant/thermal dispersion in urban areas, it is indispensable to validate CFD by comparing calculated results with reliable experimental data. In this chapter, a wind tunnel experimental technique for gas/thermal dispersion was explained, and some results of validation studies on large eddy simulation of pollutant/thermal dispersion in non-isothermal boundary layer were introduced.

Acknowledgments The author is greatly indebted to his postdoctoral researchers, PhD students, and master students for developing the measuring technique and conducting wind tunnel experiments and CFD simulations included in this chapter. Related members of this chapter are as follows.

Hideyuki Tanaka, Taich Shirasawa, Guoyi Jiang, Tingting Hu, Tsuyoshi Kobayashi, Koudai Katada, and Keisuke, Nomura.

References

- Abe S, Tamura T, Nakayama H (2008) LES on turbulence structures and gaseous dispersion behavior in convective boundary layer with the capping inversion. *J Wind Eng* 33
- Architectural Institute of Japan (2007) Guide book for practical applications of CFD to pedestrian wind environment in urban areas, Maruzen Company, Limited
- Brillant G, Husson S, Bataille F, Ducros F (2008) Study of the blowing impact on a hot turbulent boundary layer using thermal large eddy simulation. *Int J Heat Fluid Flow* 29:1670–1678

- Druault P, Lardeau S, Bonnet JP, Coiffet F, Delville J, Lamballais E, Largeau JF, Perret L (2004) Generation of three-dimensional turbulent inlet conditions for large eddy simulation. *AIAA J* 42(3):447–456
- Hattori H, Houra T, Nagano Y (2007) Direct numerical simulation of stable and unstable turbulent thermal boundary layers. *Int J Heat Fluid Flow* 28:1262–1271
- Iizuka S, Murakami S, Tsuchiya N, Mochida A (1999) LES of flow past 2D cylinder with imposed inflow turbulence. In: *Proceedings of 10th international conference on wind engineering 2*, Copenhagen, pp 1291–1298
- ISO (1993) *Guide to the expression of uncertainty in measurement*, Genève
- Jiang G, Yoshie R, Shirasawa T, Jin X (2012) Inflow turbulence generation for large eddy simulation in non-isothermal boundary layers. *J Wind Eng Ind Aerodyn* 104–106:369–378
- Kataoka H (2008) Numerical simulations of a wind-induced vibrating square cylinder within turbulent boundary layer. *J Wind Eng Ind Aerodyn* 96:1985–1997
- Kataoka H, Mizuno M (2002) Numerical flow computation around aeroelastic 3D square cylinder using inflow turbulence. *Wind Struct* 5:379–392
- Kondo K, Murakami S, Mochida A (1997) Generation of velocity fluctuations for inflow boundary condition of LES. *J Wind Eng Ind Aerodyn* 67/68:51–64
- Kong H, Choi H, Lee JS (2000) Direct numerical simulation of turbulent thermal boundary layers. *Phys Fluids* 12:2555–2568
- Lund TS, Wu XH, Squires KD (1998) Generation of turbulent inflow data for spatially-developing boundary layer simulations. *J Comput Phys* 140:233–258
- Maruyama T, Rodi W, Maruyama Y, Hiraoka H (1999) Large eddy simulation of the turbulent boundary layer behind roughness elements using an artificially generated inflow. *J Wind Eng Ind Aerodyn* 83:381–392
- Nagano Y, Kim C (1988) A two-equation model for heat transport in wall turbulent shear flows. *Trans ASME, J Heat Transf* 110:583–589
- Nozawa K, Tamura T (2002) Large eddy simulation of the flow around a low-rise building immersed in a rough-wall turbulent boundary layer. *J Wind Eng Ind Aerodyn* 90:1151–1162
- Nozawa K, Tamura T (2005) Large eddy simulation of wind flows over large roughness elements. In: *Proceedings of EACWE4, Prague*, pp 1–6
- Ohya Y (2001) Wind-tunnel study of atmospheric stable boundary layers over a rough Surface. *Bound-Lay Meteorol* 98:57–82
- Ohya Y, Uchida T (2004) Laboratory and numerical studies of the convective boundary layer capped by a strong inversion. *Bound-Lay Meteorol* 112:223–240
- Ohya Y, Uchida T (2008) Laboratory and numerical studies of the atmospheric stable boundary layers. *J Wind Eng Ind Aerodyn* 96:2150–2160
- Okaze T, Mochida A (2014) A generation method for turbulent fluctuation of wind velocity and scalar based on Cholesky decomposition of turbulent fluxes, Generation of inflow turbulence including scalar fluctuation for LES Part 1. *J Environ Eng (Trans AIJ)* 79(703):771–776
- Perret L, Delville J, Manceau R, Bonnet JP (2006) Generation of turbulent inflow conditions for large eddy simulation from stereoscopic PIV measurements. *Int J Heat Fluid Flow* 27:576–584
- Tabor GR, Baha-Ahmadi MH (2010) Inlet conditions for large eddy simulation: a review. *Comput Fluids* 39:553–567
- Tamura T (2008) Towards practical use of LES in wind engineering. *J Wind Eng Ind Aerodyn* 96:1451–1471
- Tamura T, Tsubokura M, Cao S, Furusawa T (2003) LES of spatially-developing stable/unstable stratified turbulent boundary layers. *Direct Large Eddy Simul* 5:65–66
- Tamura T, Nakayama J, Ohta K, Takemi T, Okuda Y (2006) LES estimation of environmental degradation at the urban heat island due to densely-arrayed tall buildings. In: *17th symposium on boundary layers and turbulence*, AMS, San Diego, pp 22–25
- Tominaga Y, Mochida A, Yoshie R, Kataoka H, Nozu T, Yoshikawa M, Shirasawa T (2008a) AIJ guidelines for practical applications of CFD to pedestrian wind environment around buildings. *J Wind Eng Ind Aerodyn* 96:1749–1761

- Tominaga Y, Mochida A, Murakami S, Sawaki S (2008b) Comparison of various revised k- ϵ models and LES applied to flow around a high-rise building model with 1:1:2 shape placed within the surface boundary layer. *J Wind Eng Ind Aerodyn* 96:389–411
- Xie ZT, Castro IP (2008) Efficient generation of inflow conditions for large eddy simulation of street-scale flows. *Flow, Turbul Combust* 81:449–470
- Yoshie R, Hu T (2013) Effect of atmospheric stability on urban pollutant concentration. In: Proceedings of the eighth Asia-Pacific conference on wind engineering, Chennai
- Yoshie R, Mochida A, Tominaga Y, Kataoka H, Harimoto K, Nozu T, Shirasawa T (2007a) Cooperative project for CFD prediction of pedestrian wind environment in Architectural Institute of Japan. *J Wind Eng Ind Aerodyn* 95:1551–1578
- Yoshie R, Tanaka H, Shirasawa T (2007b) Technique for simultaneously measuring fluctuating velocity, temperature and concentration in non-isothermal flow. In: Proceedings of the 12th International conference on wind engineering, Cairns, pp 1399–1406
- Yoshie R, Jiang GY, Shirasawa T, Chung J (2011) CFD simulations of gas dispersion around high-rise building in non-isothermal boundary layer. *J Wind Eng Ind Aerodyn* 99:279–288